J. Fluid Mech. (1986), *vol.* 172, *pp.* 329–345
Printed in Great Britain

Numerical studies of steady flow dispersion at low Dean number in a gently curving tube

By MARK JOHNSON AND ROGER D. KAMM
Massachusetts Institute of Technology, Cambridge, MA 02139, USA

(Received 26 August 1985 and in revised form 16 May 1986)

Using both Monte Carlo and numerical techniques, Taylor dispersion in a curved tube at low Dean numbers has been evaluated and the results are in qualitative agreement with those found by Janssen (1976): Dn^2Sc is the controlling parameter with D_{eff} falling to about 0.2 of its straight-tube value at high values of Dn^2Sc. Agreement with available experimental data is generally good. Further, we find that for large Dn^2Sc, the transition from convective to diffusive dispersion occurs earlier than in straight-tube flow, but only by a factor of two.

1. Introduction

Taylor (1953) first described the process by which the rate of axial dispersion of a solute transported by laminar flow in a straight, circular tube is reduced by radial diffusion. This process, commonly known as Taylor dispersion, has since been studied in a wide variety of flow situations, but primarily when the flow was purely in the axial direction. Additional complexity arises when secondary flows such as are found in curved tubes are also present. In such cases, lateral mixing due to molecular diffusion is augmented by the convective secondary motions.

Flow in curved or coiled tubes is important in a number of diverse applications. Helical coils are often employed in devices for heat and mass exchangers due both to their compactness and to the higher transfer coefficients they offer. The dispersion that occurs while a solute flows through such a system is of particular interest in chromatographic columns where peak broadening can occur in tubing leading to or from the column, in helical coils used as a configuration for chemical reactions (where it is desirable to reduce axial dispersion) and in systems where the molecular diffusion coefficient is measured using Taylor's method (these systems are usually coiled). Dispersion in curved tubes is also of physiological interest due to the prevalence in the circulatory and respiratory system of curved and bifurcating vessels.

2. Previous work

Dean (1927, 1928) first presented the solution for flow through a curved tube with small curvature ratio (ratio of tube diameter to helical coil diameter); his solution includes the induced secondary flow field caused by centrifugal forces but does not account for the geometric effects of streamline curvature. Under such conditions, Dean found that a single dimensionless quantity, the Dean number, determines the flow field. Following recent convention we define the Dean number as follows:

$$Dn = \left(\frac{a}{b}\right)^{\frac{1}{2}} Re, \tag{1}$$

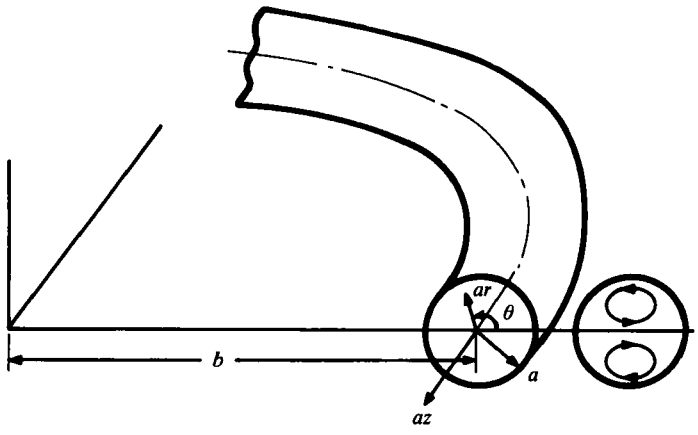

FIGURE 1. Coordinate system for curved tube. a is the tube radius and r is the dimensionless radial location. z is a dimensionless axial length. Note that the secondary flow runs directly across the tube when $\theta = 0$.

where a is the pipe radius, b is the coil radius and Re is the Reynolds number based on pipe diameter.

Dean obtained a perturbation series solution for the secondary flow stream function (ψ) and the axial velocity profile (v_z) in terms of Dn, the first term of which is thought to adequately describe the flow field for $Dn < 17$ (Ruthven 1971). In this paper, we use only the first term of Dean's solution:

$$\left.\begin{aligned} \psi &= Dn^2 f(r) \sin\theta, \\ v_z - 2(1-r^2) &= Dn^2 g(r) \cos\theta, \end{aligned}\right\} \tag{2a}$$

where r is the normalized radial coordinate (with the tube boundary at $r = 1$) as defined in figure 1. Axial velocity (v_z) is normalized by the average axial velocity ($\bar{V}$), and the secondary flow velocities ($v_r = (1/r)\,\partial\psi/\partial\theta$ and $v_\theta = -\partial\psi/\partial r$) have been normalized by ν/a where ν is the kinematic viscosity. $f(r)$ and $g(r)$ were found by Dean to be:

$$\left.\begin{aligned} f(r) &= (4r - 9r^3 + 6r^5 - r^7)/72, \\ g(r) &= (19r - 40r^3 + 30r^5 - 10r^7 + r^9)/1440. \end{aligned}\right\} \tag{2b}$$

Erdogan & Chatwin (1967) were the first to use Dean's solution for the calculation of Taylor dispersion in a curved tube. Their solution, however, consists only of the leading-order term of a series expansion and is therefore of limited applicability and can only predict under what conditions Taylor's straight-tube solution remains valid for flow in a curved tube. Nunge, Lin & Gill (1972) examined laminar dispersion in a curved tube using the velocity distribution of Topakoglu (1967) that relaxes Dean's constraint that the curvature ratio be much less than one. Despite this improvement, the results of Nunge *et al.* suffer from the same limitations as those of Erdogan & Chatwin. In a more recent numerical study, Janssen (1976) determined the steady-state effective diffusion coefficient for flow in a curved tube under conditions where (2a) is valid. His results will be discussed below.

We present here the results from two numerical simulations which examine the effect of secondary flow on axial dispersion using Dean's solution as described in (2) for Schmidt numbers ($Sc = \nu/\kappa$ where κ is the molecular diffusion coefficient) between 1 and 1000. The use of Dean's solution limits our results to $Dn < 17$ and $a/b < 0.02$. The first model described uses Monte Carlo techniques to investigate both the

transient and steady-state behaviour of the axial dispersion process; the second model provides a numerical solution for the steady-state concentration profiles and yields a more accurate prediction of the axial dispersion coefficient.

3. Monte Carlo model

3.1. *Description of the model*

The dispersion process for cases of low Dean number is described by the convection–diffusion equation written here in dimensionless form:

$$\frac{\partial c}{\partial \tau}+Sc\left[v_r\frac{\partial c}{\partial r}+\frac{v_\theta}{r}\frac{\partial c}{\partial \theta}\right]+Pe\left[v_z\frac{\partial c}{\partial z}\right]=\nabla^2 c, \tag{3}$$

where τ is dimensionless time ($\tau = \kappa t/a^2$) and Pe is the Péclet number based on tube radius. We model molecular diffusion as a Monte Carlo process adopting an approach that has been successfully used by others to model Taylor dispersion in turbulent (Allen 1982) and oscillatory (Jimenez & Sullivan 1984) flow conditions.

The numerical procedure involves a sequential solution of the convective and the diffusive parts of (3) at each timestep. The initial condition is a 'bolus' injection – a collection of 'particles' (usually 500) is distributed randomly in the cross-sectional plane. At each subsequent timestep, particles are first diffused and then convected. A particle's diffusive displacement is selected at random from a spherical Gaussian probability distribution. Particles displaced to locations outside the tube are reflected back inside. The convective displacement is determined by the axial and secondary velocity associated with the current location of the particle. Axial motion of each particle is computed using an Euler differencing scheme. An Euler differencing scheme was originally used for particle convection around the secondary flow streamlines, but it was found to contain a secular error causing all particles to migrate toward the wall. To minimize this tendency, secondary motions were computed with a second-order difference equation:

$$z(\tau+\Delta\tau)=z(\tau)+v_z(\tau)\,\Delta\tau+\tfrac{1}{2}[v_z(\tau+\Delta\tau)-v_z(\tau)]\,\Delta\tau. \tag{4}$$

The first and second moments of the axial distribution of particles can be calculated as a function of time, and the effective axial diffusion coefficient (D_{eff}) found from the rate of change of the variance:

$$D_{\text{eff}}=\frac{\Delta\sigma_x^2}{2\Delta T}. \tag{5}$$

Here ΔT is the total time interval over which D_{eff} is being measured and x is the dimensional displacement, az.

Several criteria were used to determine the appropriate timesteps ($\Delta\tau$) between particle movements. The expected radial diffusive motion (Δr) at each timestep ($\Delta r = (4\Delta\tau)^{\frac{1}{2}}$) was constrained to be less than 5% of the tube radius yielding the constraint:

$$\Delta\tau < 6.25\times10^{-4}. \tag{6}$$

We also required that the maximum convective displacement due to the secondary flow during $\Delta\tau$ be less than 5% of the tube radius. The maximum secondary flow velocity ($v_{\max}$) for the first term of Dean's perturbation solution is:

$$v_{\max}=0.014\,Dn^2, \tag{7}$$

giving the constraint:

$$\Delta\tau<\frac{3.57}{Dn^2Sc}. \tag{8}$$

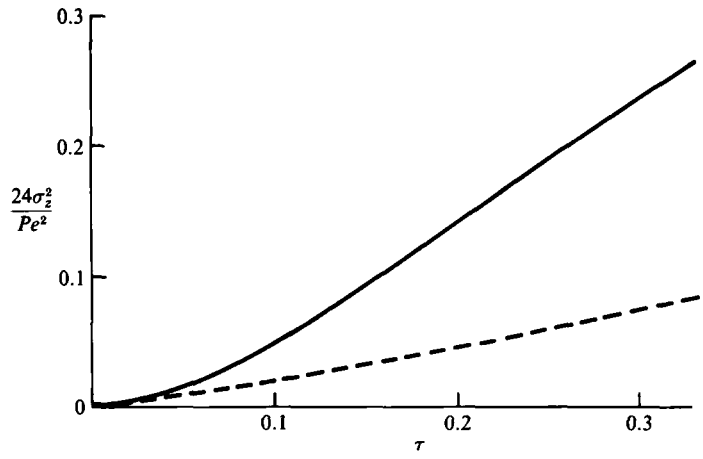

FIGURE 2. Normalized axial variance of the particle distribution as a function of non-dimensional time. The curve is normalized to give a final slope of one for dispersion in a straight circular tube. Solid line is for $Dn^2Sc = 7.27$ in which case the secondary flow is negligible; dashed line is for $Dn^2Sc = 7273$ showing significant effects of secondary flow.

A second convective constraint comes from a limitation on the numerical diffusion caused by the differencing scheme used to move the particle along the secondary flow streamlines. The numerical diffusion was constrained to be, at most, 5% of the molecular diffusion at each timestep yielding:

$$\Delta\tau < \frac{137}{[Dn^2Sc]^{\frac{6}{5}}}. \tag{9}$$

The most stringent of the constraints (6), (8) and (9) was used to determine the timestep. In practice, timesteps of approximately half of this value were used.

Due to the stochastic nature of the solution procedure, the value of D_{eff} thus obtained will naturally be a statistical quantity. A statistical analysis to determine the expected standard deviation ($\sigma_{D_{\text{eff}}}$) of the effective diffusion coefficient as a function of number of particles (N_{p}) yields:

$$\sigma_{D_{\text{eff}}} \sim O\left[\frac{5}{N_{\text{p}}}\right]^{\frac{1}{2}} D_{\text{eff}}. \tag{10}$$

The numerical results confirmed this estimate.

D_{eff} was calculated using (5) at two times sufficiently far apart that they were statistically independent of one another. No advantage was found in schemes employing multiple determinations of D_{eff} over this same time interval.

D_{eff} as defined by (5) varies with time until all particles have randomly sampled all available axial velocities. Thereafter D_{eff} is constant as indicated by the region on figure 2 where the variance varies linearly with time. For Taylor's solution in a straight tube, this lateral 'mixing time' is about $0.15a^2/\kappa$ (Chatwin 1970, value derived from analysis); for flow in a curved tube this timescale is somewhat reduced due to the secondary flow. In general, we ran twice this long to ensure that the endpoints used to calculate D_{eff} were statistically independent of one another.

The timescale for lateral mixing can be determined in several ways. The most obvious method is to identify the point at which the variance first becomes linear in time; in practice, however, this proves to be difficult to determine. Alternately,

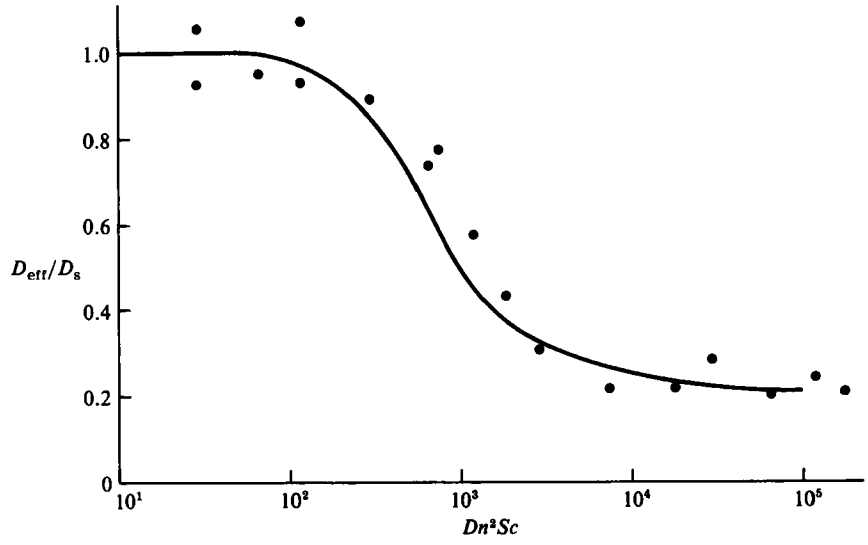

FIGURE 3. D_{eff}/D_s as a function of Dn^2Sc. Closed circles are predictions from Monte Carlo model (using 500 particles). The solid line is the prediction of the spectral model.

an auto-correlation coefficient can be computed relating the current cross-sectional position of each particle to its original cross-sectional position. When this correlation coefficient approaches zero, the particles are well-mixed. If $P_n(t)$ represents the cross-sectional position of particle n at time t, $\bar{P}$ the mean cross-sectional position of all particles, and $\sigma(t)$ the standard deviation of the cross-sectional positions, then the auto-correlation coefficient (r_c) is defined as:

$$r_c = \frac{\sum_{n=1}^{N_p} (P_n(t)-\bar{P})(P_n(0)-\bar{P})}{\sigma(t)\,\sigma(0)}. \tag{11}$$

Two correlation coefficients were calculated: one relating the original radial location of a particle to its current radial location; a second relating the original secondary flow streamline on which the particle was travelling to the current one. The first correlation coefficient is useful for finding the uncorrelation time (time for the particle position to become uncorrelated with its original position) in the absence of secondary flow. We assume this uncorrelation time to be directly related to the lateral mixing time. As secondary flow develops, this coefficient is less appropriate because the particles change their radial position as they follow the streamline, yet their position should (without diffusion) remain correlated with their original position. For this case, the second correlation coefficient (based on secondary flow stream function) becomes more appropriate.

3.2. *Results*

A series of numerical experiments were conducted, varying Dn from 0 to 13.5 and Sc from 1 (gas) to 1000 (liquid). For each of these runs, the variance of particle axial position was determined as a function of time (e.g. figure 2). Using (5), the steady-state effective diffusivity was then calculated. Figure 3 shows the steady-state values of D_{eff} (closed circles) found from these numerical experiments. The results of the Monte Carlo model are roughly concordant with those of the spectral model (solid line)

described next. Observed differences can be ascribed to the variability inherent in the Monte Carlo technique as indicated in (10).

The abscissa of figure 3 is the dimensionless parameter Dn^2Sc the significance of which was first noted by Janssen (1976). Dn^2Sc can be thought of as a secondary flow Péclet number as it represents a ratio of timescales for secondary flow and radial diffusion. For $Dn^2Sc < 100$, diffusion dominates transport in the cross-sectional plane and D_{eff} equals the straight tube result (D_s). As Dn^2Sc increases, secondary flow takes on more significance and D_{eff} falls. This continues until D_{eff} drops to about one-fifth of its straight-tube value for $Dn^2Sc > 10^4$.

For $Dn^2Sc < 100$, the secondary flow is negligible and thus, the radial correlation coefficient is appropriate. As seen in figure 4(*a*), the uncorrelation time is in good agreement with the straight-tube value predicted by Chatwin ($0.15a^2/\kappa$). For $Dn^2Sc > 10^4$, the correlation coefficient based on stream function was used and, as seen in figure 4(*b*), the uncorrelation time falls to approximately one-half of its straight-tube value. For Dn^2Sc in between these two limits, neither correlation coefficient adequately represents the correlation of a particle's cross-sectional position to its original position. However, by reviewing the plots of variance *vs.* time (e.g. figure 2), we find that the uncorrelation time (t_*) can be related to D_{eff} approximately as:

$$\frac{(t_*)_{\text{curved}}}{(t_*)_{\text{straight}}} = \left[\frac{D_{\text{eff}}}{D_s}\right]^{\frac{1}{2}}. \tag{12}$$

The Monte Carlo simulation allowed considerable versatility in examining the dispersion process. To ascertain that the results were entirely due to the secondary flow field and not to changes in the axial velocity distribution, we performed a simulation with the Dean axial velocity profile replaced with the Poiseuille profile and found no difference in the results. Changes in D_{eff} are thus due exclusively to secondary flow.

Although the axial velocity profile changes little from a Poiseuille profile, the effective axial profile seen by a particle might be quite different than the Poiseuille profile: as the particle travels around its secondary flow streamline very rapidly, it tends to move forward at the average axial velocity of that streamline. By assigning to each location an effective axial velocity equal to the average streamline axial velocity (this is actually a weighted average, weighted in inverse proportion to the secondary flow velocity of each location on the streamline), the profile deviates significantly from the Poiseuille profile. For the first term of Dean's perturbation solution, this distribution can be approximated by:

$$v_z = 1.65\left[\frac{\psi}{\psi_{\max}}\right]^{0.323}. \tag{13}$$

Here ψ is the value of the secondary flow stream function at a particular location with $\psi(r = 1) = 0$.

This modified axial velocity profile was used in the Monte Carlo simulation, while simultaneously setting all secondary flow velocities to zero. This simulation examines the influence of the effective axial velocity distribution on axial transport while preventing the enhanced mixing due to secondary flow. In this case D_{eff}/D_s was reduced to about 0.4 demonstrating that the effective axial flow profile generated by the secondary flow is responsible for much of the reduction in D_{eff} caused by the secondary flow, but that other effects are also important.

The particles were then allowed to rotate around the secondary flow streamlines,

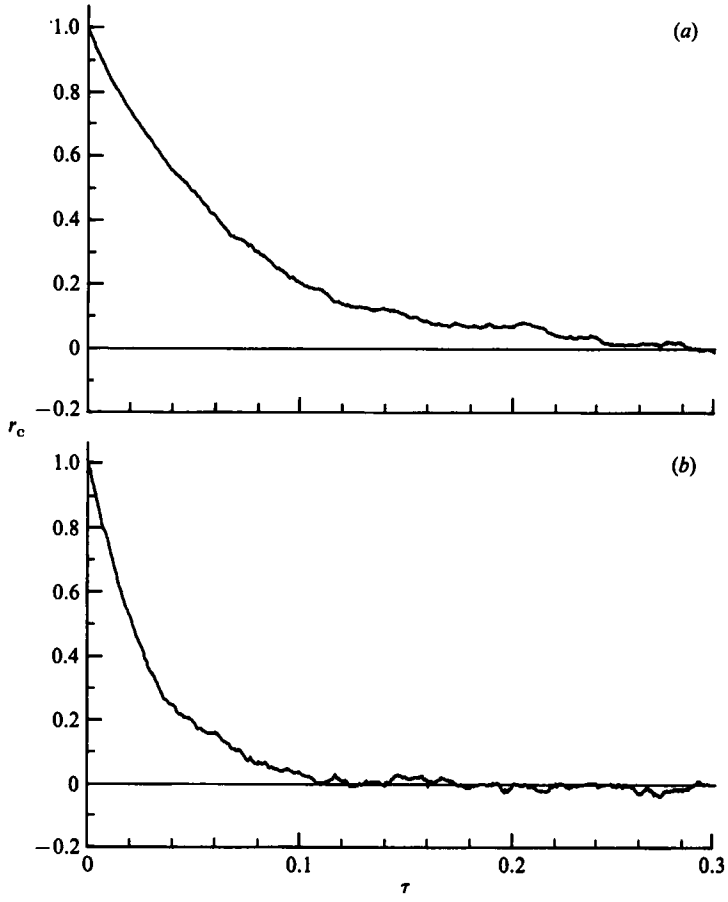

FIGURE 4. Correlation coefficient as a function of non-dimensional time. (*a*) negligible secondary flow; (*b*) high secondary flow.

but the axial flow profile was still that described in (13). For $Dn^2Sc > 10^4$, the results obtained in this manner are indistinguishable from those using Dean's solution, thus indicating that variations in the axial velocity of a particle as it travels around its secondary flow streamline are unimportant at high values of Dn^2Sc. The reduction in $D_{\text{eff}}/D_{\text{s}}$ from 0.4 to the value seen on figure 3 must then be due to enhanced mixing induced by the particles moving around the secondary flow streamlines. Thus secondary flows act to decrease D_{eff} both by enhanced mixing and by alterations of the *effective* axial velocity profile.

4. Spectral model

4.1. *Method of analysis*

We now seek a quasi-steady solution of (3). Following the approach taken by Taylor (1953), axial molecular diffusion is neglected and the equations are rewritten in a reference frame moving at the mean axial velocity. The resulting equation is assumed quasi-steady and the axial concentration gradient is assumed linear and independent of r and θ:

$$Sc\left[v_r\frac{\partial c}{\partial r}+\frac{v_\theta}{r}\frac{\partial c}{\partial \theta}\right]+Pe(v_z-1)\frac{\partial c}{\partial z}=\nabla^2_{r,\theta}c. \tag{14}$$

The Poiseuille axial velocity profile is used consistent with the finding above that the small change in axial flow profile due to curvature at low Dn has little effect on D_{eff}. Introducing a dimensionless concentration:

$$\chi = \frac{c}{Pe(\partial c/\partial z)},$$

and incorporating (2) into (14) yields:

$$Dn^2Sc\left[\frac{f(r)}{r}\cos\theta\frac{\partial\chi}{\partial r} - \frac{f'(r)}{r}\sin\theta\frac{\partial\chi}{\partial\theta}\right] + \tfrac{1}{2}(1-2r^2) = \nabla^2_{r,\theta}\chi. \tag{15}$$

Using a finite difference technique, Janssen (1976) solved (15) subject to the boundary conditions: (i) the concentration as the tube centre ($r = 0$) is finite, and (ii) the mass flux at the wall is zero. It was with this second boundary condition that Janssen discovered a problem. He was able to demonstrate that the differential equation to be solved always satisfies the solvability condition:

$$\int_0^{2\pi}\left.\frac{\partial\chi}{\partial r}\right|_{r=1} d\theta = 0. \tag{16}$$

As Dn^2Sc approaches zero, $\partial\chi/\partial r$ is independent of θ, and (16), which the governing differential equation always satisfies, becomes identical to the zero flux boundary condition at the wall. Thus the applied boundary conditions leave the problem underspecified at low values of Dn^2Sc. Janssen attempted to correct this difficulty by introducing an additional wall boundary condition, but was then unable to precisely satisfy $\partial\chi/\partial r = 0$ at the wall for high values of Dn^2Sc.

Our method of solution employs a Fourier cosine series to describe the concentration distribution that successfully avoids this difficulty:

$$\chi(r,\theta) = c_0(r) + c_1(r)\cos\theta + c_2(r)\cos 2\theta + \ldots. \tag{17}$$

Equation (17) is substituted in (15) with the following result:

$$\sum_{n=0}^{\infty}\left[c_n'' + \frac{1}{r}c_n' - \frac{n^2}{r^2}c_n\right]\cos n\theta - \tfrac{1}{2}\mathcal{A}\nu^2\Sigma\chi\sum_{n=0}^{\infty}\left[f(r)\,c_n' + \frac{g(r)}{r}nc_n\right]\cos(n-1)\theta$$

$$-\tfrac{1}{2}Dn^2Sc\sum_{n=0}^{\infty}\left[f(r)\,c_n' - \frac{g(r)}{r}nc_n\right]\cos(n+1)\theta = \tfrac{1}{2}(1-2r^2). \tag{18}$$

We then multiply (18) by $\cos m\theta$ and integrate from 0 to π, obtaining for each value of m, a distinct equation (see Appendix A). Truncating the series after N terms, we obtain $N+1$ ordinary differential equations for the coefficients $c_n(r)$, $n = 0, 1, \ldots, N$.

The first boundary condition requires that the concentration at $r = 0$ is finite. Therefore, all the coefficients $c_n(r)$ must remain finite at $r = 0$. For c_0, equation (A 1) dictates that as $r \to 0$, the term $(1/r)\,c_0'$ dominates. Thus we require

$$\frac{dc_0(r=0)}{dr} = 0. \tag{19}$$

For $n > 0$, equations (A 2) and (A 3) show the dominant term to be n^2c_n/r^2 as $r \to 0$. Therefore, we require

$$c_n(r=0) = 0 \quad (n > 0). \tag{20}$$

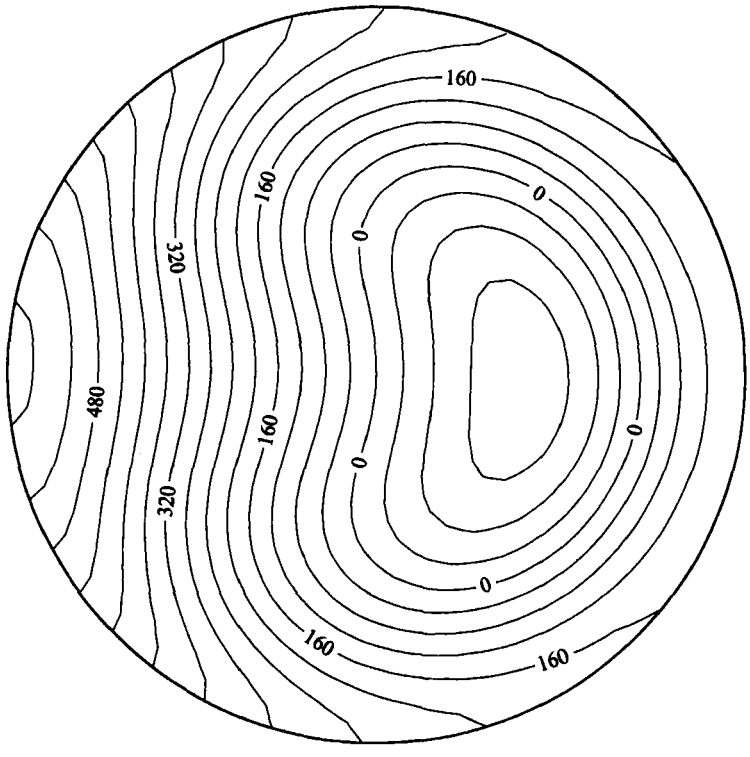

FIGURE 5. Dimensionless concentration profile for $Dn^2Sc = 717$. For figures 5–8, the centre concentration is arbitrarily set to zero.

The second boundary condition is that of zero flux at the wall:

$$\frac{dc_n(r=1)}{dr} = 0 \quad \text{for all } n. \tag{21}$$

Since the series is truncated for all $n > N$, equations (19)–(21) represent $2(N+1)$ boundary conditions for the $N+1$ second-order differential equations derived from (18). If (17) is now substituted into the constraint (equation (16)) we find:

$$\frac{dc_0(r=1)}{dr} = 0, \tag{22}$$

which is identical to the $n = 0$ boundary condition of (21). Therefore, this system is underdetermined in the same sense as that encountered by Janssen. We can however, eliminate this indeterminacy by requiring:

$$c_0(r=0) = 0, \tag{23}$$

which merely specifies the mean concentration at a particular cross-section.

To solve this set of differential equations, a second-order finite differencing scheme was used:

$$r = m\Delta r \quad (m = 0 \text{ to } M). \tag{24}$$

$M+1$ nodes were placed in the radial direction (M was usually set equal to twenty). Using a central differencing scheme (see Appendix A) to replace the derivatives in

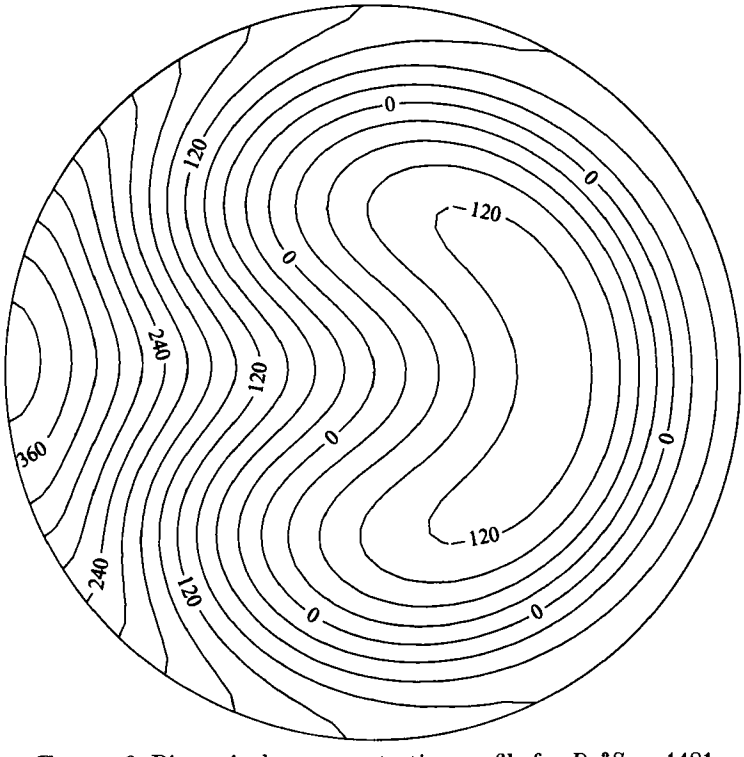

FIGURE 6. Dimensionless concentration profile for $Dn^2Sc = 1481$.

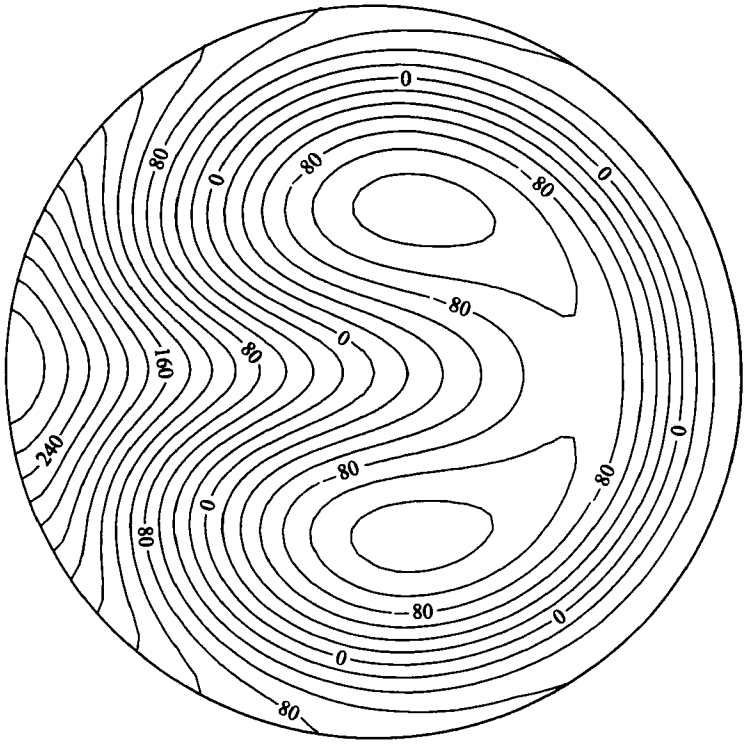

FIGURE 7. Dimensionless concentration profile for $Dn^2Sc = 2764$.

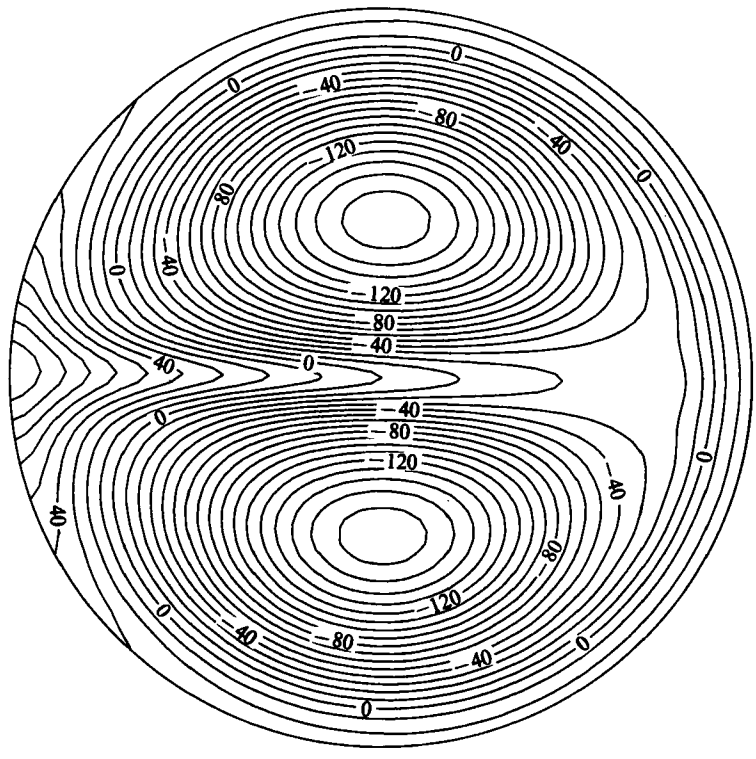

FIGURE 8. Dimensionless concentration profile of $Dn^2Sc = 25 \times 10^4$.

equations (A 1)–(A 3), an algebraic equation was obtained at each of the internal nodes: $m = 1$ to $M-1$. For $m = 0$ and $m = M$, the boundary conditions (19)–(23) were used. Derivatives were replaced with second-order forward or backward differences. Thus $M+1$ equations were obtained for each of the spectral modes ($n = 0$ to N), and a set of $(M+1)(N+1)$ algebraic equations was obtained. Gaussian elimination with full pivoting was used to invert the resulting matrix.

To determine how many spectral modes were required to describe the concentration distribution, c_N (the concentration of the highest spectral mode) was constrained to be at most 1 % of c_0. For $Dn^2Sc < 2500$, $N = 10$. For $Dn^2Sc > 2500$, N was increased with Dn^2Sc up to a maximum of $N = 30$ at $Dn^2Sc = 10^5$.

From the concentration profiles thus obtained the steady-state effective diffusivity is found, using:

$$D_{\text{eff}} = \frac{-1}{(\pi a^2)\,\partial c/\partial x} \int_{r=0}^{1} \int_{\theta=0}^{2\pi} \overline{V}(v_z - 1)\, c(r,\theta,z)\, a^2 r \,\mathrm{d}r \,\mathrm{d}\theta, \tag{25}$$

or, in dimensionless form:

$$\frac{D_{\text{eff}}}{\kappa} = -\frac{Pe^2}{\pi} \int_{r=0}^{1} \int_{\theta=0}^{2\pi} (1-2r^2)\, \chi(r,\theta,z)\, r \,\mathrm{d}r \,\mathrm{d}\theta. \tag{26}$$

Using (17) and recalling Taylor's result for a straight tube, we find:

$$\frac{D_{\text{eff}}}{D_{\text{s}}} = -96 \int_{r=0}^{1} (1-2r^2)\, c_0(r)\, r \,\mathrm{d}r. \tag{27}$$

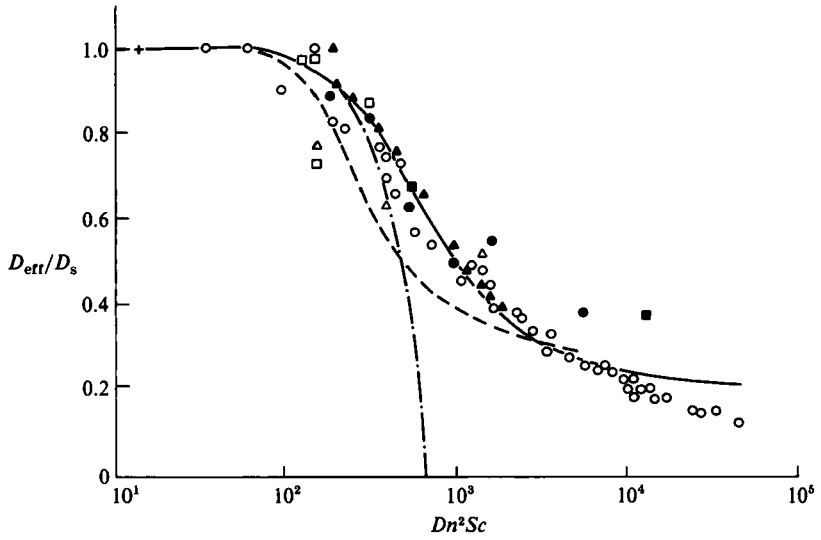

FIGURE 9. D_{eff}/D_s as a function of Dn^2Sc. The experimental data points are from □, van Andel *et al.* (1964), ■, Trivedi & Vasudeva (1975); △, Nigam & Vasudeva (1976); ●, Shetty & Vasudeva (1977); ○, van den Berg & Deelder (1979); and ▲, Andersson & Berglin (1981). The solid line is the prediction of the spectral model; the dashed line is from Janssen (1976); the dot–dashed line is from Erdogan & Chatwin (1967).

Note that this result depends only on $c_0(r)$, a direct consequence of replacing the Dean axial velocity profile (which is θ-dependent) with the Poiseuille profile.

4.2. *Results*

The concentration profile and steady-state effective diffusion coefficients were found for Dn^2Sc between 0 and 10^5. Figures 5–8 show the concentration profiles for Dn^2Sc of 717, 1481, 2764 and 25×10^4. As the secondary flow increases, the concentration profiles first become skewed toward the outer wall of the bend. At $Dn^2Sc \approx 2000$, the concentration profiles break into two cells. As Dn^2Sc is further increased, the concentration profiles take on an appearance which strongly resembles the secondary flow stream function.

The solid line on figure 9 shows the values of D_{eff} computed from these concentration profiles; the dashed line is from the numerical model of Janssen (1976) and the dot–dash line is the prediction of the perturbation method of Erdogan & Chatwin (1967). Janssen's model and the spectral model described here give qualitatively the same results, but as discussed in the next section, the predictions of the spectral model more closely approximate the published experimental results; the spectral model also shows better agreement with the analytical prediction of Erdogan & Chatwin.

4.3. *Asymptotic limit for high Dn^2Sc*

The results shown in figure 9 indicate that D_{eff} asymptotically approaches a constant value for high values of Dn^2Sc. We therefore examined the asymptotic behaviour of (14) and found that as $Dn^2Sc \to \infty$, the isoconcentration lines and streamlines coincide. Consequently, we can write:

$$\frac{\partial c}{\partial \eta} = K(\psi)\frac{\partial \psi}{\partial \eta}, \tag{28}$$

where η is in the direction normal to the streamlines and $K(\psi)$ is a function yet to be determined. To find D_{eff}, (14) is integrated over an area A, bounded by a streamline to obtain:

$$Pe \int_A (v_z - 1) \frac{\partial c}{\partial z} \, \mathrm{d}A = \int_A \nabla^2 c \, \mathrm{d}A. \tag{29}$$

Using (28) and Gauss's theorem, we find:

$$Pe \int_A (v_z - 1) \, \mathrm{d}A = K(\psi) \int_A \nabla^2 \psi \, \mathrm{d}A. \tag{30}$$

Equations (30) and (2) determine $K(\psi)$ which, through (28), establishes the concentration profile. Finally, (25) is used to find D_{eff}. The result obtained using the first term of Dean's perturbation series indicates that $D_{\text{eff}}/D_{\text{s}} \to 0.20$ as $Dn^2Sc \to \infty$, as is indicated by figure 9 (still subject to the constraint that $Dn < 17$).

5. Comparison with experimental data

Numerous investigators have measured the steady-state effective diffusion coefficient for flow in helical coils. In many cases however, the data for large values of Dn^2Sc are suspect because the coiled tubes used were not long enough to allow a steady-state to be reached. The length of the tube used is a measure of the time available for dispersion. In order to obtain a reliable measurement of D_{eff} using (5), both variance measurements must be made for $\tau > 0.15$; however, in most measurement systems, the standard deviation of the axial concentration profile is measured at a single location, and D_{eff} is assumed to have been constant since $\tau = 0$. This assumption is justified only when $\tau > 0.8$ (Shetty & Vasudeva 1977). A second inaccuracy stems from the non-Gaussian nature of the concentration–time profile. Even if D_{eff} is constant over the entire flow period and thus the peak is Gaussian in space, it will not necessarily be Gaussian in time at a fixed measurement site. The criterion for the peak to be nearly Gaussian in time can be shown to be (see Appendix B)

$$Pe_L = \frac{\bar{V}L}{D_{\text{eff}}} \gg 1, \tag{31}$$

where Pe_L is a Péclet number based on the length of the tube (L) and D_{eff}. The criterion in (31) can be shown to be of similar form to the requirement that $\tau > 0.8$; therefore in figure 9 are shown all available data for conditions satisfying this criterion (with $Dn < 17$).

Although the agreement between the numerical model and experimental data is generally good, one feature stands out: at high values of Dn^2Sc, the data do not approach the limit suggested by the model, although the data do show some tendency to level off. Other results (Trivedi & Vasudeva 1975, van den Berg & Deelder 1979), with $\tau < 0.8$ also show a tendency to drop below the limits suggested by the various models.

6. Discussion

Using both Monte Carlo and numerical techniques, Taylor dispersion in a curved tube at low Dean number has been evaluated and the results are in qualitative agreement with those found by Janssen: Dn^2Sc is the controlling parameter with $D_{\text{eff}}/D_{\text{s}} \to 0.20$ for large values of Dn^2Sc. This result explains the different dispersion

behaviours for gases and liquids at identical Dean numbers. Further, we find that for large Dn^2Sc, the transition from convective to diffusive dispersion occurs earlier than in a straight tube, but only by a factor of two, contrary to the conclusion by Trivedi & Vasudeva (1975) that the transition time continues to fall with increasing Dn. The mixing time does not continue to fall because at high Dn^2Sc the iso-concentration pattern approaches the streamline pattern and becomes independent of the magnitude of Dn^2Sc.

The Monte Carlo simulations allow an evaluation of the mechanism by which flow in a curved tube changes the effective diffusivity. Several timescales are associated with the transverse mixing process: the circulation time of a particle travelling around a secondary flow streamline, the time for mixing in a direction normal to the streamlines, and the time for mixing along a streamline (Rhines & Young 1983). At high Dn^2Sc, the circulation time and the time for mixing along a streamline are small compared to the time for mixing across streamlines. In this limit, due to rapid motion along the secondary flow streamlines, the streamlines and isoconcentration lines coincide as discussed above and thus the time for mixing across streamlines dominates the process. For intermediate values of Dn^2Sc, there exists a range for which the timescales are comparable and the different mixing mechanisms interact, producing the transition in $D_{\text{eff}}/D_{\text{s}}$ from 1.0 to 0.2.

The Monte Carlo simulation indicated that the principal effects of secondary flows were a modification of the *effective* axial velocity profile to that of the streamline average, and increased mixing due to diffusion between adjacent streamlines. It is also interesting that the leading-order changes in the axial velocity profile from that of a Poiseuille profile do not (without secondary flow) have any effect on the effective diffusivity at the low Dean numbers considered here.

The regions of small differences between our models and the data can probably be explained by numerical or experimental inaccuracies; however, the differences seen for $Dn^2Sc > 10^4$ seem more significant. As three different theoretical techniques have all substantially agreed that the curve of figure 4 should asymptote to about 0.20 for $Dn^2Sc > 10^4$, we might look for differences between the experimental and theoretical conditions. The models all assume not a helix, but a curved tube continuously curving in a single plane. Small deviations from this idealized geometry, due either to the helical arrangement found in most experiments, or to slight variations in the tube cross-sectional shape or radius of curvature might contribute some degree of randomness to the flow. The resultant mixing across secondary flow streamlines could cause a progressive reduction in D_{eff} consistent with the experimental data. An additional assumption inherent in the model is that the tube curvature only enters the problem through the Dean number. Nunge *et al.* (1972) have shown that differences in local path length caused by the curvature can only increase D_{eff}. Since the experimental data is lower than our prediction, this is unlikely to be a factor.

To obtain a better understanding of the source of these differences, additional experiments should be conducted at higher values of Dn^2Sc under conditions in which D_{eff} is known to be constant. The use of two detection sites, both sufficiently far downstream to ensure that $\tau > 0.15$, would eliminate the problems discussed earlier. In comparison with systems designed for a single detector with $\tau > 0.8$, the tubing length could be reduced by more than 50 % while yielding more accurate results.

The authors wish to thank Professors Ascher Shapiro and Anthony Patera of the Massachusetts Institute of Technology for their suggestions and comments concerning this study. This work was supported by NSF Grant no. 8313017-MEA and NHLBI Grant P01-HL-33009.

Appendix A

Using a Fourier cosine transformation over the interval $[0, \pi]$, equation (18) can be transformed into the following set of equations:

$$c_0'' + \frac{c_0'}{r} - \tfrac{1}{2}Dn^2Sc\left[f(r)\,c_1' + \frac{g(r)}{r}\,c_1\right] = \tfrac{1}{2}(1-2r^2), \tag{A 1}$$

$$c_1'' + \frac{c_1'}{r} - \frac{c_1}{r^2} - \tfrac{1}{2}Dn^2Sc\left[f(r)\,c_2' + \frac{g(r)}{r}\,2c_2\right] - \tfrac{1}{2}Dn^2Sc[2f(r)\,c_0'] = 0, \tag{A 2}$$

$$c_n'' + \frac{c_n'}{r} - \frac{n^2c_n}{r^2} - \tfrac{1}{2}Dn^2Sc\left[f(r)\,c_{n+1}' + \frac{g(r)}{r}\,(n+1)\,c_{n+1}\right]$$

$$-\tfrac{1}{2}Dn^2Sc\left[f(r)\,c_{n-1}' - \frac{g(r)}{r}\,(n-1)\,c_{n-1}\right] = 0. \tag{A 3}$$

Equations (A 1)–(A 3) are then solved using a second-order differencing scheme:

$$c_n'(m\Delta r) = \frac{c_n^{m+1} - c_n^{m-1}}{2\Delta r}, \tag{A 4}$$

$$c_n''(m\Delta r) = \frac{c_n^{m+1} - 2c_n^m + c_n^{m-1}}{\Delta r^2}. \tag{A 5}$$

At the boundaries ($m = 0$ or $m = M$), derivatives were calculated using three-point differencing schemes:

$$c_n'(0) = \frac{-3c_n^0 + 4c_n^1 - c_n^2}{2\Delta r}, \tag{A 6}$$

$$c_n'(M\Delta r) = \frac{3c_n^M - 4c_n^{M-1} + c_n^{M-2}}{2\Delta r}. \tag{A 7}$$

Appendix B. Time moments of the axial dispersion of a Gaussian profile for flow in a tube

We consider here the axial dispersion of a solute assuming the effective diffusivity is independent of time from the beginning of the dispersion process. Such a case is not physically realistic (except for low Péclet number in which case molecular diffusion is the dominant dispersive process), but allows us to evaluate the inaccuracy inherent in assuming that a Gaussian spread of concentration in space is also Gaussian in time at a fixed measurement location. Under these conditions, relative to the mean axial position, the solute disperses in a Gaussian fashion:

$$c(x^*, t) = \frac{B}{2(\pi D_{\text{eff}}\,t)^{\frac{1}{2}}} \exp\left[-\frac{(x^*)^2}{4D_{\text{eff}}\,t}\right], \tag{B 1}$$

were B is the amplitude of the original Gaussian peak. Note here that although the peak is Gaussian in space (x^*), it is not Gaussian in time (t). By evaluating the

temporal moments, we will show that only under certain conditions is the profile nearly Gaussian in time.

We define a new variable x such that $x = x^* + \bar{V}t$, where $\bar{V}$ is the mean axial velocity and x is the coordinate fixed in space. Substituting this into (B 1), and specifying a measurement site at $x = L$, we find that:

$$c(L,t) = \frac{B}{2(\pi D_{\text{eff}}\, t)^{\frac{1}{2}}} \exp\left[-\frac{(L-\bar{V}t)^2}{4D_{\text{eff}}\, t}\right]. \tag{B 2}$$

(B 2) determines the various moments in time of the concentration distribution measured at $x = L$. To facilitate this calculation, the following definitions are introduced:

$$Pe_L = \frac{\bar{V}L}{D_{\text{eff}}},$$

$$t_n = \frac{\int_{t=0}^{\infty} t^n c(L,t)\, \mathrm{d}t}{\int_{t=0}^{\infty} c(L,t)\, \mathrm{d}t}.$$

Performing the indicated operations yields the following results:

$$\left.\begin{aligned} t_1 &= \frac{L}{\bar{V}}\left[1+\frac{2}{Pe_L}\right], \\ t_2 &= \frac{Pe_L^2 D_{\text{eff}}^2}{\bar{V}^4}\left[1+\frac{6}{Pe_L}+\frac{12}{Pe_L^2}\right]. \end{aligned}\right\} \tag{B 3}$$

Since the solute moves at the same average velocity as does the solvent, (B 3) shows that only for large Pe_L can t_1 be used to calculate the average solute velocity. Calculating the variance we obtain:

$$\sigma_\tau^2 = t_2 - t_1^2. \tag{B 4}$$

If the peak is Gaussian in both time and space, then their respective variances can be related through the following expression:

$$\frac{\sigma_t^2}{t_1^2} = \frac{\sigma_x^2}{L^2}. \tag{B 5}$$

If we calculate the ratio of the time variance to the square of the mean transit time (using (B 3) and (B 4)), we find:

$$\frac{\sigma_t^2}{t_1^2} = \frac{2}{Pe_L}\frac{(1+4/Pe_L)}{(1+2/Pe_L)^2}. \tag{B 6}$$

For a Gaussian peak, the variance in space can be shown to be (van Andel, Kramers & De Voogd 1964):

$$\frac{\sigma_x^2}{L^2} = \frac{2D_{\text{eff}}\, t_1}{L^2}. \tag{B 7}$$

Therefore, we find that (B 6) yields the correct value for the variance only when $Pe_L \gg 1$. Otherwise a correction factor must be applied when calculating the effective diffusivity using the variance and assuming a Gaussian distribution. Specifically, if

D^*_{eff} is the value for the effective diffusivity found assuming the peak to be Gaussian in time, then the actual effective diffusivity is found to be:

$$D_{\text{eff}} = D^*_{\text{eff}} \frac{(1+2/Pe_L)^3}{(1+1/Pe_L)}, \tag{B 8}$$

if D_{eff} has been constant during the dispersion process.

REFERENCES

ALLEN, C. 1982 Numerical simulation of contaminant dispersion in estuary flows. *Proc. R. Soc. Lond.* A **381**, 179–194.

VAN ANDEL, E., KRAMERS, H. & VOOGD, A. 1964 The residence time distribution of laminar flow in curved tubes. *Chem. Engng Sci.* **19**, 77–78.

ANDERSSON, B. & BERGLIN, T. 1981 Dispersion in laminar flow through a circular tube. *Proc. R. Soc. Lond.* A **337**, 251–268.

VAN DEN BERG, J. H. M. & DEELDER, R. S. 1979 Measurement of axial dispersion in laminar flow through coiled capillary tubes. *Chem. Engng Sci.* **34**, 1345–1347.

CHATWIN, P. C. 1970 The approach to normality of the concentration distribution of a solute in a solvent flowing in a straight pipe. *J. Fluid Mech.* **43**, 321–352.

DEAN, W. R. 1927 Note on the motion of fluid in a curved pipe. *Phil. Mag.* S7 **4**, 208–223.

DEAN, W. R. 1928 The streamline motion of fluid in a curved pipe. *Phil. Mag.* S7 **5**, 673–695.

ERDOGAN, M. E. & CHATWIN, P. C. 1967 The effects of curvature and buoyancy on the laminar dispersion of solute in a horizontal tube. *J. Fluid Mech.* **29**, 465–484.

JANSSEN, L. A. M. 1976 Axial dispersion in laminar flow through coiled tubes. *Chem. Engng Sci.* **31**, 215–218.

JIMENEZ, C. & SULLIVAN, P. J. 1984 Contaminant dispersion in some time-dependent laminar flows. *J. Fluid Mech.* 57–77.

NIGAM, K. D. P. & VASUDEVA, K. 1976 Influence of curvature and pulsations on laminar dispersion. *Chem. Engng Sci.* **31**, 835–837.

NUNGE, R. J., LIN, T.-S. & GILL, N. 1972 Laminar dispersion in curved tubes and channels. *J. Fluid Mech.* **51**, 363–383.

RHINES, P. B. & YOUNG, W. R. 1983 How rapidly is a passive scalar mixed within closed streamlines? *J. Fluid Mech.* **133**, 133–145.

RUTHVEN, D. M. 1971 The residence time distribution for ideal laminar flow in a helical tube. *Chem. Engng Sci.* **26**, 1113–1121.

SHETTY, V. D. & VASUDEVA, K. 1977 Effect of Schmidt number on laminar dispersion in helical coils. *Chem. Engng Sci.* **32**, 782–783.

TAYLOR, G. I. 1953 Dispersion of soluble matter in solvent flowing slowly through a tube. *Proc. R. Soc. Lond.* A **219**, 186–203.

TOPAKOGLU, H. C. 1967 Steady laminar flows of an incompressible viscous fluid in curved pipes. *J. Math. Mech.* **16**, 1321–1338.

TRIVEDI, R. N. & VASUDEVA, K. 1975 Axial dispersion in laminar flow in helical coils. *Chem. Engng Sci.* **30**, 317–325.